
Article:
Zhao, Xing orcid.org/0000-0003-4000-0446 and Niu, Shuangxia (2019) A New Slot-PM Vernier Reluctance Machine With Enhanced Zero-Sequence Current Excitation for Electric Vehicle Propulsion. IEEE Transactions on Industrial Electronics. pp. 3528-3539. ISSN 0278-0046

https://doi.org/10.1109/TIE.2019.2920600

This article has been accepted for publication in a future issue of this journal, but has not been fully edited. Content may change prior to final publication. Citation information: DOI 10.1109/TIE.2019.2920600, IEEE Transactions on Industrial Electronics

A New Slot-PM Vernier Reluctance Machine with Enhanced Zero Sequence Current Excitation for Electric Vehicle Propulsion

Xing Zhao, and Shuangxia Niu *IEEE Senior Member,*

***Abstract*—This paper aims to propose a new Vernier reluctance machine (VRM), which integrates the advantages of a robust rotor structure, good torque density and flexible flux control ability. The key is to establish the excitation field with both stator slot PMs and zero-sequence current. Two excitation sources have different pole pair numbers but share a parallel magnetic circuit and contribute to superimposed torque in this machine. Meanwhile, a flexible flux control can be achieved by regulating zero-sequence current, and little demagnetization risk exists for slot PMs during flux control. In this paper, the machine configuration and operation principle are introduced, along with its integrated AC and DC drive method. Electromagnetic performance of this new machine is evaluated by finite element analysis. Leading design parameters are determined and optimized considering optimal injection ratio of zero-sequence current. A prototype is fabricated, and relevant experiment results demonstrate the feasibility of the proposed solution.**

***Index Terms*—Integrated AC and DC drive, slot PMs, Vernier reluctance machine, zero-sequence current.**

I. Introduction

In modern electric vehicles (EV), using direct-drive machine to provide propulsion power has been regarded as one important trend, since it brings distinct vehicle-level advantages such as improved dynamic index due to fast torque response, enlarged inner space by elimination of mechanical transmission devices, and higher efficiency of the whole propulsion system [1]. Since the EV working condition of changes frequently, a direct-drive machine should be designed to work efficiently during a whole driving cycle. Specifically, it should have good torque density for low-speed starting, low torque ripple for stable driving, and excellent flux weakening ability for high-speed cruising.

In the past several years, a variety of machine topologies are investigated for EV propulsion. The interior permanent magnet machine (IPM), which utilizes both permanent magnet (PM) torque and reluctance torque, has attracted much attention due to its excellent torque density and flux weakening ability [2-3]. However, IPM has relatively large torque ripple ratio caused by non-sinusoidal PM air-gap field [4]. The surface-mounted PM machine (SPM) is another solution. By reasonably configuring the slot pole combination of SPM, excellent torque density, low cogging torque and torque ripple ratio, can be simultaneously achieved in SPM [5]. However, the flux weakening operation is still a tough issue for SPM due to its zero saliency-effect [6-7]. Further, SPM with a consequent-pole rotor (CP-SPM) becomes an emerging topology, which achieves almost the same torque density as that of conventional SPM with 33% reduced PMs [8]. However, some issues still need to be solved in CP-SPM, such as even-order air gap harmonics and axial leakage flux [9-10]. Vernier PM machine (VPM) is a promising topology, which has been widely investigated for its excellent torque density arising from intrinsic magnetic gearing effect [11]. Compared to IPM and SPM, power factor of VPM is relatively disadvantageous due to large armature inductance. Apart from abovementioned topologies, another kind of design, namely stator PM machines in which the PM source is arranged at stator side, becomes a potential solution for EV propulsion benefiting from its robust mechanical structure and wide speed range [12-13]. However, one distinct drawback for stator PM machines is low torque density, which restricts their practical applications [14].

With the development of flux modulation theory in the past several years [15-17], it is revealed that for stator PM machines including flux reversal PM machine (FRPM) and flux switching PM machine (FSPM), their operation modes can be interpreted from a unified perspective of flux modulation principle [18-19]. Based on this, a variety of new stator PM machine topologies are derived out with improved torque density for direct-drive applications. For instance, in [20], a new FRPM topology with a consequent-pole PM array is proposed for EV propulsion, in which the pole-to-pole leakage flux is reduced effectively and thus its torque density is boosted. In [21], a novel FSPM with overlapping winding is designed with enhanced torque density. However, its torque ripple ratio is relatively severe due to rich back emf harmonics. Very recently, in [22], a new dual-excited Vernier reluctance machine (VRM) is proposed, which utilizes both DC wound source and slot PM source to achieve enhanced torque density. However, the space conflict between DC coils and AC coils should be further addressed.

Inspired by the integrated design of AC and DC windings by zero-sequence current control as that reported in [23], this paper proposes a new slot-PM VRM with integrated design of AC and DC windings for EV propulsion. The proposed machine utilizes zero-sequence current to function as the DC field excitation and establish a parallel magnetic field with slot PM source. In this way, enhanced torque performance can be achieved since dual excitation sources can work synchronously. Besides, a flexible flux control can be realized by adjusting zero-sequence current, giving a benefit to the speed range extension. Meanwhile, there is little demagnetization risk for slot PMs during flux control.

This paper is organized as follows. In Section II, the machine configuration, operation principle and the integrated drive method based on zero-sequence current control, are introduced firstly. In Section III, feasible slot pole combinations are stuided considering both the drive circuit and electromagnetic torque. In Section IV, performance of this new machine is fully evaluated by finite element analysis. In Section V, the influence of leading design parameters on average torque, torque ripple ratio and loss distribution, is studied comprehensively. Design optimization is performed with consideration of optimal zero-sequence current ratio. In Section VI, a prototype is built and tested. Some conclusions are drawn in Section VII.

Manuscript received August 22, 2018; revised October 10, 2018; December 28, 2018; March 18, 2019; accepted May 17, 2019. This work was supported by Project No. 152509/16E under the Research Grant Council, Hong Kong, and Project No. 51707171 under National Natural Science Foundation, China

Xing Zhao and Shuangxia Niu are both with the Department of Electrical Engineering, The Hong Kong Polytechnic University, Hong Kong, China. (Corresponding author: Shuangxia Niu; e-mail: eesxniu@polyu.edu.hk)

This article has been accepted for publication in a future issue of this journal, but has not been fully edited. Content may change prior to final publication. Citation information: DOI 10.1109/TIE.2019.2920600, IEEE Transactions on Industrial Electronics

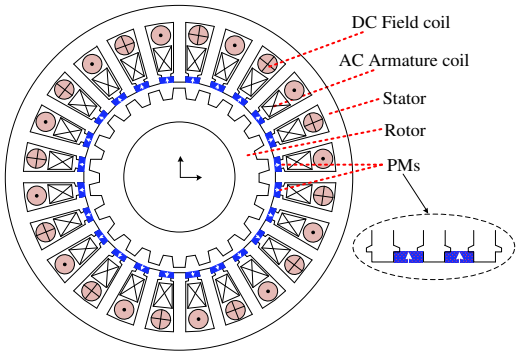

Fig. 1. Structure of the dual-excited VRM in [22].

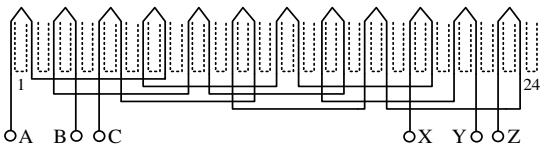

Fig. 2. Connection of AC armature winding.

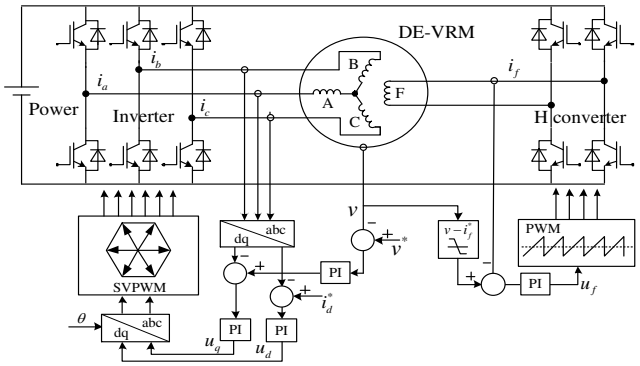

Fig. 3. Drive circuit for dual-excited VRM.

II. Proposed New VRM Drive System

A. Dual-excited Vernier reluctance machine

Fig. 1 presents the configuration of the proposed dual-excited Vernier reluctance machine (DE-VRM) in [22]. It consists of a 24-slot stator and a 22-pole-pair rotor. The rotor consists of only iron, and thus providing mechanical robustness. Two excitation sources are located at stator side, one is DC field source and the other is slot PM source. The PMs are mounted on slot openings and they are magnetized in the same radially outward direction as denoted in Fig. 1. Although this PM array and magnetization mode are quite different from conventional PM machines, it is proved in [22] that slot PM source can provide distinct torque generation. Fig. 2 presents the connection of armature winding, which uses a single-layer concentrated configuration. The drive circuit for DE-VRM is denoted in Fig. 3, in which the DC field terminal is fed by H converter for bidirectional flux regulation.

B. Proposed VRM with integrated AC and DC winding

However, in the DE-VRM mentioned above, a distinct issue that cannot be neglected is the space conflict between DC field coils and AC armature coils since they are accommodated in the common stator slots. Therefore, a new design is proposed in this paper as presented in Fig. 4, in which the AC and DC integrated winding is used to simultaneously function as DC field winding and AC armature winding. Fig. 5 shows the connection of this integrated winding. There are six winding terminals since every phase is split into two sub-phases. A dual-inverter drive circuit in which neutral points of two sub-phase groups are connected, is employed to inject AC and DC integrated current excitation. Its control strategy is also presented in Fig. 6.

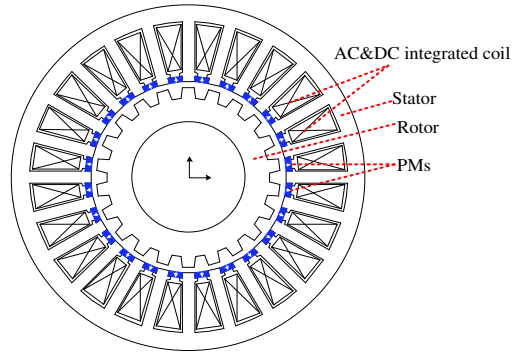

Fig. 4. Structure of the proposed VRM with integrated AC and DC coils.

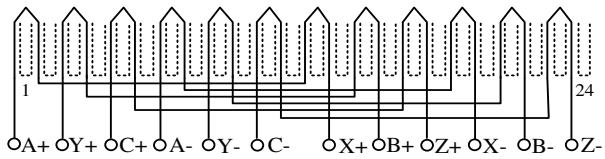

Fig. 5. Connection of integrated AC and DC winding.

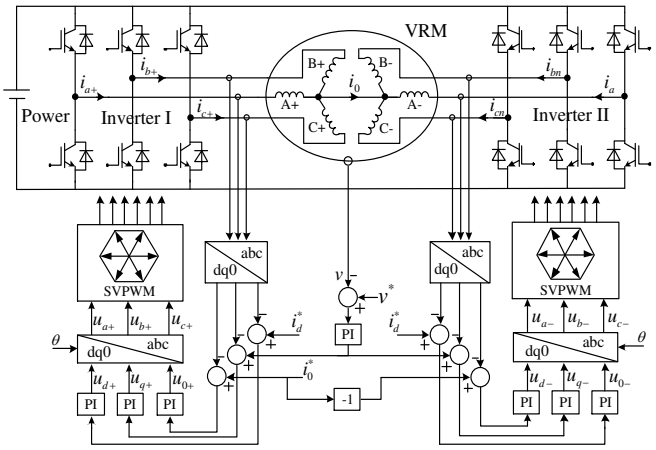

Fig. 6. Dual-inverter drive control for the proposed VRM.

Compared to DE-VRM with separated AC and DC winding, features of this new integrated design can be listed as follows.

For machine design. (1) The slot area is enlarged for both AC armature excitation and DC field excitation. Therefore, smaller copper loss will be consumed when applying the same current, leading to efficiency improvement. (2) Under the same thermal limit, larger current can be injected into AC and DC integrated windings. This contribute to enhanced torque density.

For drive circuit. (1) Two more power devices are used. (2) The current scale of each power device should be increased due to the overlap of AC and DC current. (3) The voltage scale of each power device is the same as that in separated design, since every phase winding is split into two sub-phases.

In general, this integrated design of AC and DC windings, gives a potential for machine itself to be designed with higher efficiency and higher torque density. with a little sacrifice in the cost of drive circuit and complexity of control strategy. In this paper, the influence of this integrated design on drive system is considered acceptable. Further, more efforts will be provided in machine design for electromagnetic performance boost.

This article has been accepted for publication in a future issue of this journal, but has not been fully edited. Content may change prior to final publication. Citation information: DOI 10.1109/TIE.2019.2920600, IEEE Transactions on Industrial Electronics

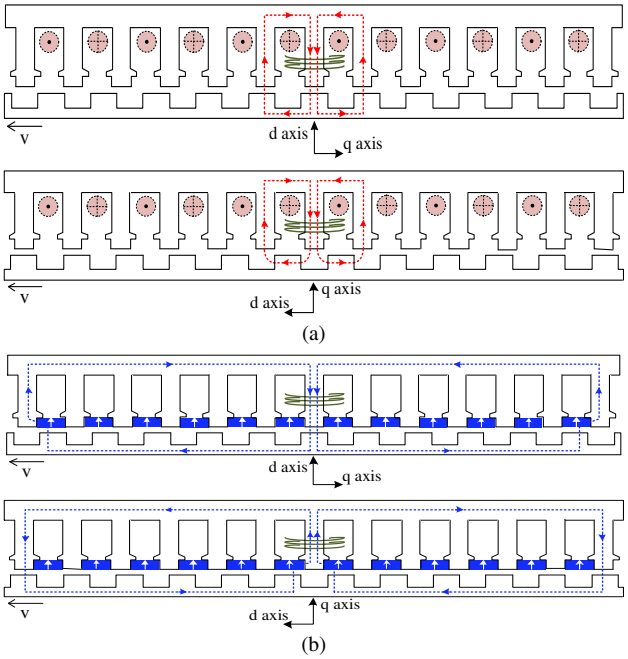

Fig. 7. Flux distribution. (a) Only virtual DC source. (b) Only slot PM source.

C. Operation principle

The operation principle of this new VRM, can be illustrated by splitting it into two individual machines as denoted in Fig. 7. One is a DC-excited doubly salient machine (DC-DSM) and the other is a slot-PM-excited VRM. As presented Fig. 7(a), in DC-DSM, excitation field is established by DC current component in the integrated winding under zero-sequence current control. This can be considered as inserting a virtual DC field winding at stator side. With the variation of rotor permeance, pulsating armature flux will be generated in DC-DSM, which contributes to reluctance torque generation. For slot-PM-excited VRM, as shown in Fig. 7(b), each slot PM and adjacent core form a pair of magnetic poles. Further, this PM excitation field at stator side is modulated by rotor permeance and interact with the armature winding. It can be found, slot PM has relatively longer magnetic return path compared to that of virtual DC source. However, the torque capacity of slot PMs is theoretically better for its bipolar flux feature. Besides, the flux linkage of two excitation sources, has the same phase angle as denoted by d-q axis in Fig. 7. Hence, torque components of two sources can effectively overlap.

The features of this new VRM can be summarized as

1) With a passive rotor configuration, this new VRM maintains a good mechanical robustness, which can reduce the risk of PM damage compared with rotor-PM-excited machines.
2) Due to a non-overlapping design, the winding ends are short, and thus end copper loss and material cost are reduced.
3) Torque components of zero-sequence current and slot PMs can effectively overlap, thus providing good torque density.
4) The magnetic return paths of zero-sequence current and slot PMs are in parallel. Hence, bidirectional zero-sequence current can be applied for wide-speed-range flux regulation. Besides, little demagnetization risk exists for slot PMs.

D. Integrated current injection

Based on the distribution principle and polarities of DC coils and AC coils in the common slots, the injected current into two sub-phase groups can be expressed as

$$\begin{cases} i_{A+} = i_{ac}\cdot\sin(\theta_e)+i_{dc} \\ i_{B+} = i_{ac}\cdot\sin(\theta_e-2\pi/3)+i_{dc} \\ i_{C+} = i_{ac}\cdot\sin(\theta_e+2\pi/3)+i_{dc} \\ i_{A-} = i_{ac}\cdot\sin(\theta_e)-i_{dc} \\ i_{B-} = i_{ac}\cdot\sin(\theta_e-2\pi/3)-i_{dc} \\ i_{C-} = i_{ac}\cdot\sin(\theta_e+2\pi/3)-i_{dc} \end{cases} \quad (1)$$

where i_{A+}, i_{B+}, i_{c+} are the current flowing from the inverter I, and i_{A-}, i_{B-}, i_{c-} are the current flowing from the inverter II. i_{ac} is the amplitude of AC current component. i_{dc} is DC current component, which functions as the virtual DC field winding in the proposed DE-VRM. θ_e is the rotor electrical angle, which can be calculated as

$$\theta_e = N_r\theta_r + \alpha \quad (2)$$

where N_r is the number of rotor pole pairs, θ_r is the mechanical angle, α is the initial electrical angle.

By using the Clarke and Park transformer matrix, the current excitation under αβ0 and dq0 coordinate system, can be written as follows, taking current from inverter I as an example.

$$\begin{bmatrix} i_{\alpha+} \\ i_{\beta+} \\ i_{\alpha\beta0+} \end{bmatrix} = \sqrt{\frac{2}{3}} \begin{bmatrix} 1 & -\frac{1}{2} & -\frac{1}{2} \\ 0 & \frac{\sqrt{3}}{2} & -\frac{\sqrt{3}}{2} \\ \frac{1}{\sqrt{2}} & \frac{1}{\sqrt{2}} & \frac{1}{\sqrt{2}} \end{bmatrix} \begin{bmatrix} i_{A+} \\ i_{B+} \\ i_{C+} \end{bmatrix} \quad (3)$$

$$\begin{bmatrix} i_{d+} \\ i_{q+} \\ i_{0+} \end{bmatrix} = \begin{bmatrix} \cos\theta_r & -\sin\theta_r & 0 \\ \sin\theta_r & \cos\theta_r & 0 \\ 0 & 0 & 1 \end{bmatrix} \begin{bmatrix} i_{\alpha+} \\ i_{\beta+} \\ i_{\alpha\beta0+} \end{bmatrix} \quad (4)$$

By substituting Eq. (1) into Eq. (3) and Eq. (4), the relationship between the zero-sequence current from the inverter I and DC current can be derived as

$$i_{0+} = \sqrt{3} i_{dc} \quad (5)$$

Similarly, the relationship between the zero-sequence current from the inverter II and DC current can be expressed as

$$i_{0-} = -\sqrt{3} i_{dc} \quad (6)$$

Based on Eq. (5) and (6), it can be found i_{dc} is proportional to the zero-sequence current flowing from inverter I to inverter II through the neutral path, which means DC current component can be effectively regulated at the armature terminal by means of controlling zero-sequence current excitation.

E. Inductance and torque characteristic

In the proposed VRM, the self-inductance of each sub-phase can be expressed as follows, using A+ as an example

$$L_{A+} = L_{dc} + \sum L_n \cdot \sin(nN_r\theta_r + \alpha),\ n = 1,2,3... \quad (7)$$

where L_{dc} is the constant self-inductance component, and L_n is the amplitude of the nth harmonic self-inductance component.

Considering the counter-cyclical characteristic in the 24-slots and 22 pole-pairs design, the self-inductance of sub-phase A- is delayed by 180° electrical angle than that of A+. Accordingly, self-inductance of A- can be written as

This article has been accepted for publication in a future issue of this journal, but has not been fully edited. Content may change prior to final publication. Citation information: DOI 10.1109/TIE.2019.2920600, IEEE Transactions on Industrial Electronics

$$L_{A-} = L_{dc} + \sum L_n \cdot \sin(nN_r\theta_r + n\pi + \alpha),\ n = 1,2,3... \quad (8)$$

Further, with a single-layer concentrated winding connection, little mutual-inductance exists between two sub-phase groups, thus the excited flux linkage by i_0 can be expressed as

$$\begin{aligned}\phi_{A\_i0} &= L_{A+} \cdot i_{dc} + L_{A-} \cdot (-i_{dc}) = i_{dc}(L_{A+} - L_{A-}) \\ &= 2i_{dc} \sum L_n \sin(nN_r\theta_r + \alpha),\ n = 1,3,5...\end{aligned} \quad (9)$$

It is shown although DC biased self-inductance and even-order harmonic self-inductance exist in each sub-phase, their effects on excited flux are cancelled for counter-cyclical characteristic. The final flux linkage generated by i_0 contains the fundamental component and all odd-order harmonics components.

The torque component excited by i_0 can be deduced as

$$T_{i0} = \frac{\mathrm{m} \cdot N_r \cdot \phi_{A\_i0} \cdot i_{ac}}{2} \quad (10)$$

where m is the number of phases. Neglecting saturation effect, the torque exited by both slot PMs and i_0 can be written as

$$T_e = T_{PM} + T_{i0} = \frac{\mathrm{m} \cdot N_r \cdot \left(\phi_{A\_PM} + \phi_{A\_i0}\right) \cdot i_{ac}}{2} \quad (11)$$

where φ_{A_PM} and T_{PM} are the flux linkage and torque excited by slot PMs, similar with that in conventional PM machines.

III. Selection of Slot Pole Combination

A. Influence on drive circuit selection

The feasible slot pole combinations in the proposed topology can be expressed as

$$\begin{cases} N_s = 2mj,\ j = 1,2,3... \\ N_r = N_s \pm 2k,\ k = 1,2,3... \end{cases} \quad (12)$$

where N_s is the number of stator slots. The odd rotor pole pairs are not considered due to the influence of unbalanced magnetic pull. Further, according to the flux modulation mechanism, N_r should be in close to N_s to achieve a relatively high pole ratio and torque density. Hence, using a 24-slot stator, four potential slot pole combinations are studied in this paper, that are 24/20, 24/22, 24/26 and 24/28, separately. The slot angle with different slot pole combinations can be deduced as

$$\gamma = \frac{360^\circ}{N_s} N_r \quad (13)$$

Further, the electrical angle difference $\Delta\theta_e$ between every two sub-phases can be calculated as

$$\Delta\theta_e = (h\gamma) \bmod (360^\circ) \quad (14)$$

where h is the interval number of slots between two sub-phases. As listed in Table I, 24/20 and 24/28 cases have the same $\Delta\theta_e$ of 0°, while 24/22 and 24/26 cases have the same $\Delta\theta_e$ of 180°. Based on the coil distribution in the proposed machine, in 24/20 and 24/28 cases, polarities of virtual DC coil and AC armature coil are consistent, while these are opposite in 24/22 and 24/26 cases. Therefore, for 24/20 and 24/28 cases, the drive circuit to inject zero-sequence current can be simplified as presented in Fig. 8, in which every two sub-phases are positively connected and fed by common DC current flowing into the neutral point of splitting capacitors. It is shown the drive circuit for 24/20 and 24/28 cases is simpler compared to 24/20 and 24/28 cases.

TABLE I
Electrical angle difference between every two sub-phases

N_s	24	24	24	24
N_r	20	22	26	28
γ	300	330	330	300
$\Delta\theta_e$	0	180	180	0

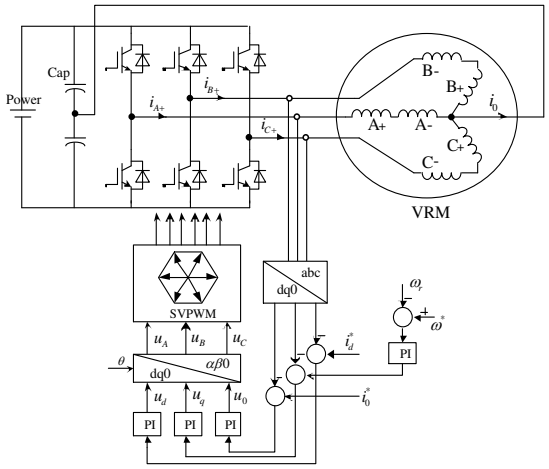

Fig. 8. Drive system for 24/20 and 24/28 design cases.

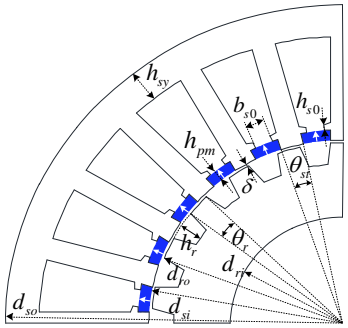

Fig. 9. Dimension parameters of the proposed machine.

TABLE II
Initial dimension parameters of the proposed machine

Symbol	Parameter	Unit	Value
d_{so}	Outer diameter of stator	mm	120
d_{si}	Inner diameter of stator	mm	69
d_{ro}	Outer diameter of rotor	mm	68.5
d_{ri}	Inner diameter of rotor	mm	20
δ	Air gap length	mm	0.5
l	Stack length	mm	50
h_{sy}	Height of stator yoke	mm	Variable
θ_{st}	Arc of stator teeth	°	Variable
θ_{pm}	Arc of slot PMs	°	Variable
h_{pm}	Height of slot PMs	mm	Variable
θ_{ro}	Outer arc of rotor poles	°	Variable
θ_{ri}	Inner arc of rotor poles	°	Variable
h_r	Height of rotor slots	mm	Variable
b_{s0}	Open width of stator slots	mm	3
h_{s0}	Height of stator shoes	mm	1

TABLE III
Major materials and specifications

PM	Material	NdFeB35
	Remanence	1.2 T
	Coercive force	915 kA/m
Steel	Material	MG19_24
	Saturated flux density	1.8 T
	Mass density	7650 kg/m^3

This article has been accepted for publication in a future issue of this journal, but has not been fully edited. Content may change prior to final publication. Citation information: DOI 10.1109/TIE.2019.2920600, IEEE Transactions on Industrial Electronics

TABLE IV
Torque performance with different slot combinations

Number of stator slots	24	24	24	24
Number of rotor pole pairs	20	22	26	28
Height of stator yoke (mm)	5	5	5	5
Arc of stator teeth (°)	7	7	7	7
Height of slot PMs (mm)	2	2	2	2
Outer arc of rotor pole (°)	9	8	6.8	6.5
Inner arc of rotor pole (°)	10	9	8	7
Height of rotor slot (mm)	4	4	4	4
Cogging torque (Nm)	0.82	0.22	0.21	0.63
Rated torque (Nm)	4.41	4.23	4.11	3.92

B. Influence on torque performance

As is well known, slot pole combination usually has a leading influence on machine performance. In the proposed design, slot PM is the dominant source for torque generation. Hence, for the initial selection process, zero-sequence current is not applied.

Finite element simulation is adopted by using the commercial software Maxwell. General dimension parameters are denoted in Fig. 9, with design values listed in Table II. The materials of PM and steel, as well as their main specifications, are given in Table III. The rotor parameters are optimized for each slot pole combination to achieve best torque performance, and the stator parameters are set unchanged to ensure the same PM usage. The design values after optimization are presented in Table IV. It is shown, 24/20 case has the largest rated torque, but its cogging torque is also distinct. When the ratio of cogging torque to rated torque is considered as the comparison indicator, 24/22 case is recommended. It should be pointed out, performance of 24/26 and 24/28 combinations is generally not comparable to that of 24/20 and 24/22 cases, which is caused by their increased PM leakage flux with reduced pole pitch.

In general, from a perspective of machine design, 24/22 case can achieve smaller cogging torque ratio than 24/20 case, while from a perspective of drive circuit, 24/22 case needs one more inverter for zero-sequence current injection compared to 24/20 case, which increases the system cost. In this paper, the machine performance is determined to have a higher design priority than system cost, and thus 24/22 case is selected to be further studied, while in cost-limited applications, 24/20 case is recommended.

IV. Electromagnetic Performance of 24/22 Design

A. No-load flux distribution and back emf

Firstly, the no-load sub-phase flux linkage of 24/22 design is calculated and plotted in Fig. 10, with corresponding harmonics distribution presented in Fig. 11. It can be noticed, when excited by only i_0 of 6A, the flux linkage generated in each sub-phase winding is unipolar and biased, while that excited by slot PMs is bipolar and alternating. As presented in Fig. 11, although rich flux harmonics exist in each sub-phase winding, the DC biased components and all even-order harmonics can be cancelled due to inner counter-cyclical characteristic.

Then, the no-load flux distribution under different excitation status is presented in Fig. 12. From Fig. 12(a), it can be seen, the main flux of i_0 will not pass through slot PMs. Meanwhile, the leakage flux of i_0 starts from the wounded stator tooth, then passing through stator pole shoes and finally comes back from stator yoke. The leakage flux of slot PMs mainly forms its loop around stator pole shoes as shown in Fig. 12(b). Further, when two excitation sources are both active as given in Fig. 12(c), the main flux of i_0 and slot PMs can overlap together, while their leakage flux around stator pole shoes can be cancelled to some extent, as is shown when comparing Fig. 12(b) and Fig. 12(c).

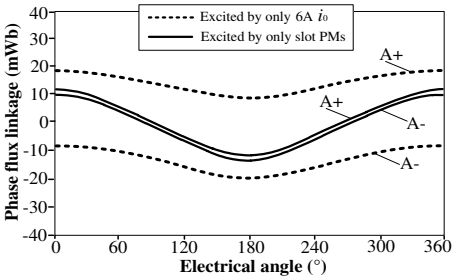

Fig. 10. No-load sub-phase flux linkage.

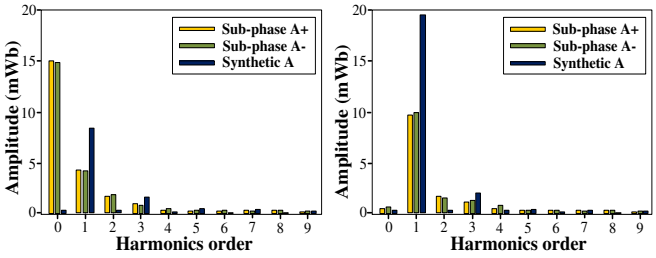

Fig. 11. Harmonics in sub-phase flux linkage (a) Only 6A i_0. (b) Only slot PM.

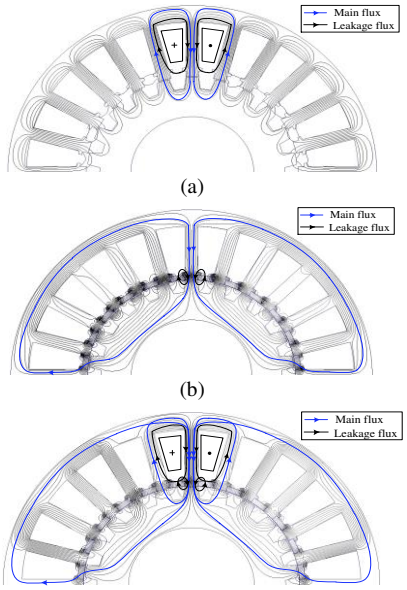

Fig. 12. Exciting field. (a) Only 6A i_0. (b) Only slot PM. (c) Slot PM and 6A i_0.

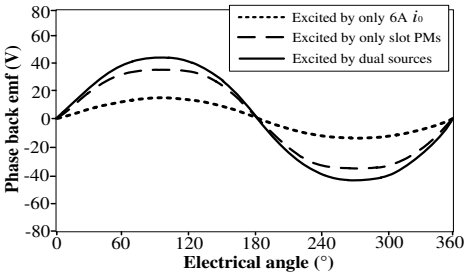

Fig. 13. No-load back emf of synthetic phase A.

The back emf of synthetic phase A is calculated and plotted in Fig.13. It can be noticed, the back emf excited by i_0 and slot PMs are entirely in phase and thus they can effectively overlap together and contribute to boosted voltage.

This article has been accepted for publication in a future issue of this journal, but has not been fully edited. Content may change prior to final publication. Citation information: DOI 10.1109/TIE.2019.2920600, IEEE Transactions on Industrial Electronics

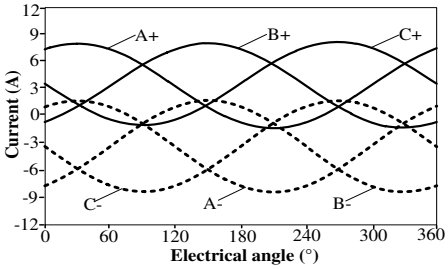

Fig. 14. Integrated AC and DC current excitation.

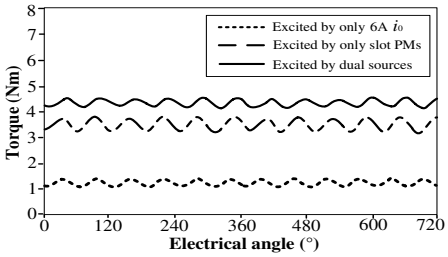

Fig. 15. Steady torque components.

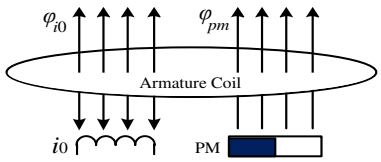

Fig. 16. Schematic flux regulation by zero-sequence current control.

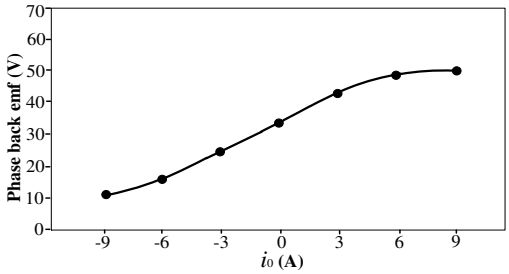

Fig. 17. No-load phase back emf with different zero-sequence current.

B. *Injected current and steady torque*

Fig. 14 presents the injected current excitation into integrated winding. Sub-phase A+ and sub-phase A- share the same AC current component with 5A amplitude and same electrical angle. However, sub-phase A+ has positive DC current of 3.5A under 6A i_0 control, while A- has negative DC current of 3.5A. Steady torque at different excitation status is calculated and presented in Fig. 15. It can be noticed, both slot PMs and i_0 can contribute to the steady torque generation. The synthetic average torque is boosted when dual excitation sources are both active, and the torque ripple ratio is mitigated to some extent, benefiting from the reduction of slot PM leakage when i_0 is applied. This torque improvement proves the validity of the proposed topology.

C. *Flux regulation ability*

As presented in Fig. 16, the flux linkage excited by i_0 is in parallel with that produced by slot PMs. Meanwhile, its polarity depends on the direction of i_0, which means, by controlling the flowing direction and amplitude of i_0, the synthetic flux linkage at armature terminal can be flexibly strengthened or weakened. This contributes to effective flux control for the speed extension. The no-load back emf curve is collected and plotted in Fig. 17, which proves that flux can be bidirectionally regulated by i_0.

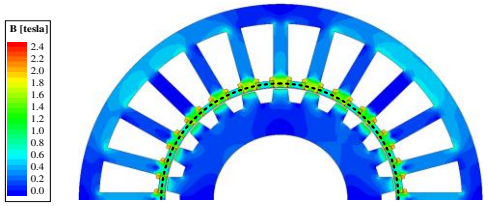

Fig. 18. Observation line for flux density distribution.

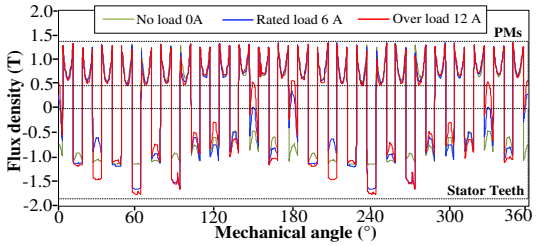

Fig. 19. Flux density at different load condition.

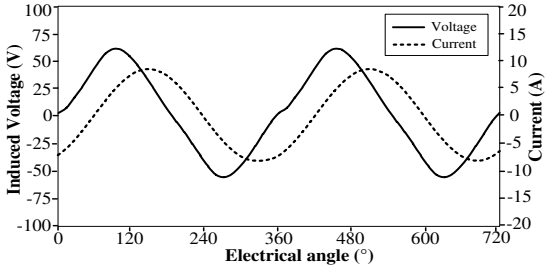

Fig. 20. Rated-load current and induced voltage.

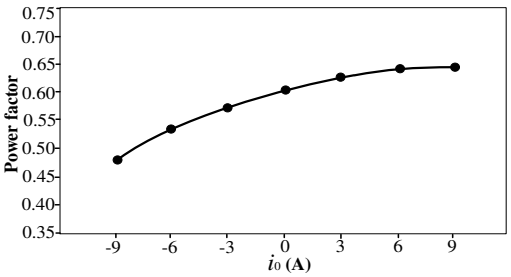

Fig. 21. Power factor with different zero-sequence current.

D. *Demagnetization risk*

To evaluate the PM demagnetization risk, an observation line is selected across the central area of PMs as denoted in Fig. 18. Then, PM flux density at different load conditions is calculated as given in Fig. 19. It is shown, with load changing, the working point of PMs keeps almost constant, while flux density in stator teeth changes distinctly. This is because PMs are placed in slots, and thus flux linkage of armature current will not pass through PMs, which contributes to a parallel magnetic circuit. Therefore, if the cooling condition is allowed, PM demagnetization risk by loading change can be avoided in the proposed machine.

E. *Power factor*

The power factor of the proposed machine at rated condition is evaluated by measuring the phase angle difference of on-load current and voltage as shown in Fig. 20. The power factor of the proposed machine at rated condition is about 0.62, which is not so good due to large magnetizing inductance, similar with that in other flux-modulated machines. Further, the influence of i_0 injection on power factor is evaluated as shown in Fig. 21. It is shown injecting positive i_0 can increase power factor slightly, benefiting from the enhanced air gap flux density.

This article has been accepted for publication in a future issue of this journal, but has not been fully edited. Content may change prior to final publication. Citation information: DOI 10.1109/TIE.2019.2920600, IEEE Transactions on Industrial Electronics

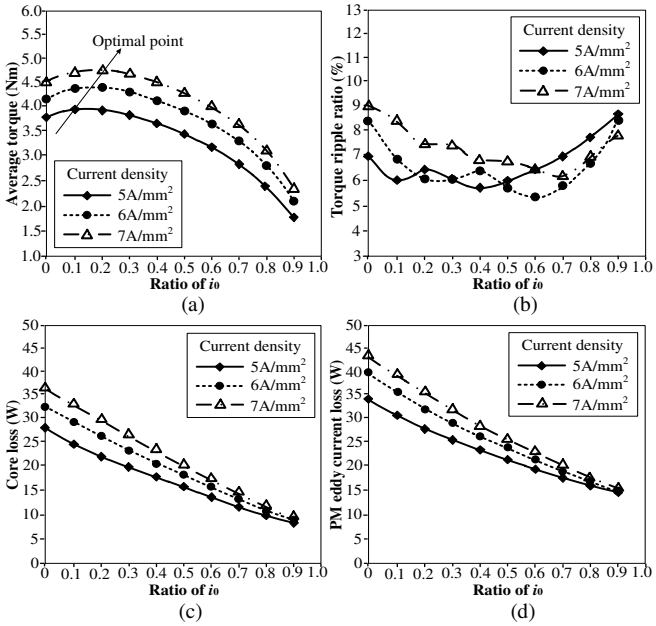

Fig. 22. Influence of current density with different ratio of i_0. (a) Average torque. (b) Torque ripple ratio. (c) Core loss. (d) PM eddy current loss.

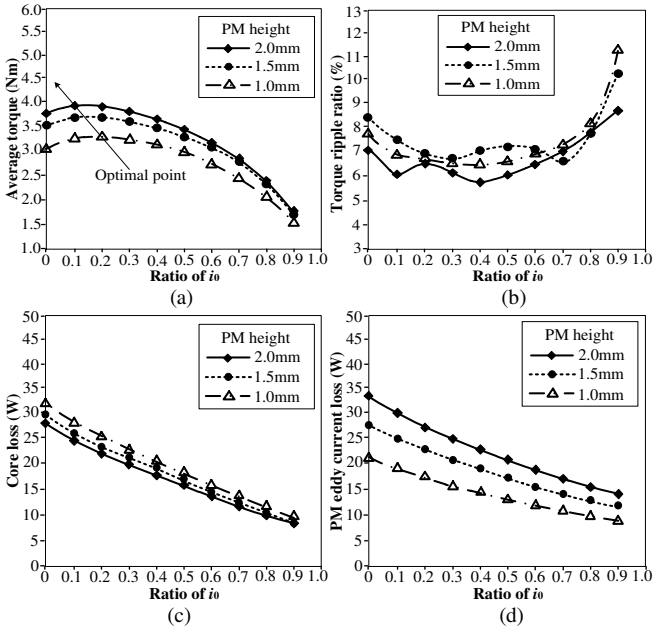

Fig. 23. Influence of PM height with different ratio of i_0. (a) Average torque. (b) Torque ripple ratio. (c) Core loss. (d) PM eddy current loss.

V. Design Optimization and Comparative Study

In the proposed machine, three control variables, i_d, i_q and i_0, should be considered at armature terminal. i_d is usually applied for reluctance torque generation based on saliency effect. In the proposed design, saliency effect is not distinct with 24-slot 22-pole-pairs combination and thus i_d is maintained at zero. Then, i_q and i_0 are combined for torque generation. The electrical load for each phase winding can be expressed as

$$i_{rms}=\sqrt{\left(i_q^2+i_0^2\right)/3} \tag{15}$$

To evaluate the machine performance with different i_q and i_0 combination, the ratio of i_0 is defined as

$$k_{i0}=i_0/\sqrt{i_q^2+i_0^2} \tag{16}$$

when the ratio of i_0 is zero, there will be only i_q injection, which is similar with that in traditional surface-mounted PM machines. In the following, the influence of leading design parameters is assessed with different i_q and i_0 combination.

A. Parameter analysis

Under different current density, the influence of ratio of i_0 on machine performance is analyzed, including the average torque, torque ripple, core loss and PM eddy current loss, as presented in Fig. 22. It is shown in Fig. 22(a), with the increase of current density from 5 to 7 A/mm^2, the optimal ratio of i_0 to achieve the highest torque increases from 9% to 18% approximately. Two reasons account for this trend. On one hand, torque excited by i_0 has a square relationship to current value, while that excited by slot PMs is linearly related, as can be found in Eq. (10). On the other hand, the torque component of slot PMs will be closed to saturation point with the increase of current density, and thus larger ratio of i_0 can work for torque generation. Under 7A/mm^2 current density, the average torque with optimal i_0 ratio is 8% higher than that with only i_q injected. Further, it can be seen in Fig. 22(b), (c) and (d), i_0 injection shows a positive influence on the mitigation of torque ripple ratio and loss distribution.

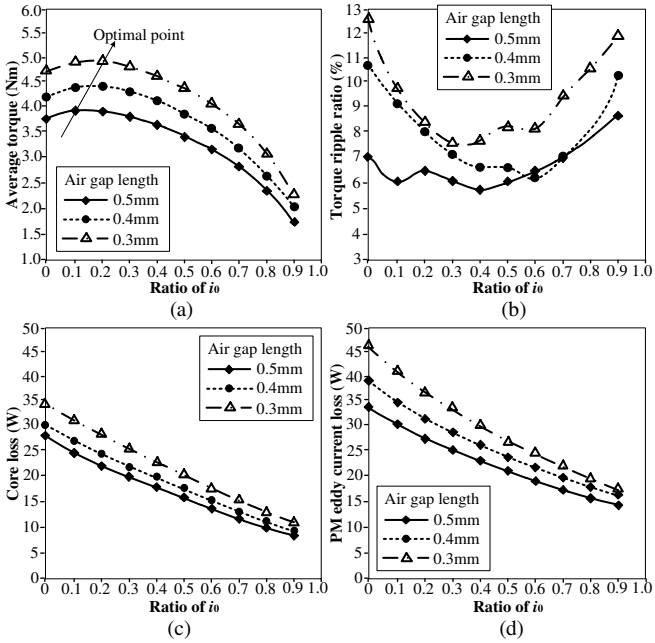

Fig. 24. Influence of air gap length with different ratio of i_0. (a) Average torque. (b) Torque ripple ratio. (c) Core loss. (d) PM eddy current loss.

The influence of PM height with different ratio of i_0, is also evaluated as shown in Fig. 23. The current density is fixed at 5 A/mm^2. With the increase of PM height, the optimal ratio of i_0 to achieve the highest torque shows decrease trend. Meanwhile, the PM height has a larger influence on eddy current loss than core loss. Further, the influence of air gap length with different ratio of i_0 is studied as shown in Fig. 24. The current density is set at 5 A/mm^2. With the decrease of air gap length, the optimal ratio of i_0 increases accordingly. This is because the excitation ability of i_0 is more sensitive to the air gap reluctance than that of PMs. From Fig. 22, 23 and 24, it can be concluded, regardless of the design parameters, injecting i_0 always presents a positive influence on the reduction of torque ripple and loss distribution, benefiting from PM leakage mitigation to some extent.

This article has been accepted for publication in a future issue of this journal, but has not been fully edited. Content may change prior to final publication. Citation information: DOI 10.1109/TIE.2019.2920600, IEEE Transactions on Industrial Electronics

TABLE V
Dimension parameters, boundary limits and optimal values

Parameters	Lower limit	Upper limit	Optimal
Height of stator yoke (mm)	4.5	9.5	6.2
Arc of stator teeth (°)	6.5	8.5	7.3
Height of slot PMs (mm)	1.5	3.5	2.2
Outer arc of rotor pole (°)	6.5	8.5	6.8
Inner arc of rotor pole (°)	6.5	10.5	8.2
Height of rotor slot (mm)	3.5	4.5	4.2

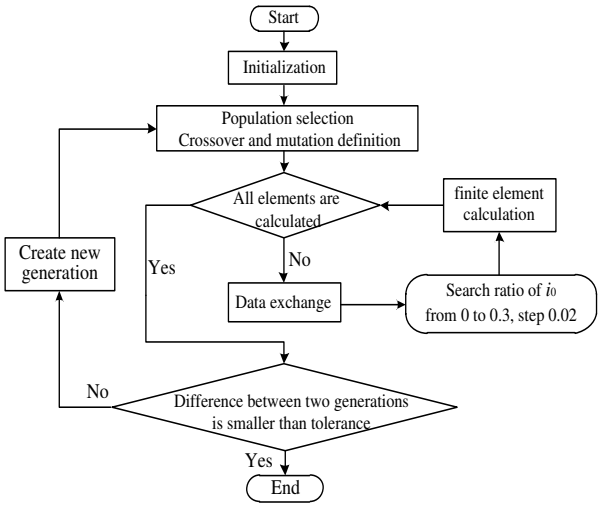

Fig. 25. Flowchart of the GA and Maxwell coupled optimization.

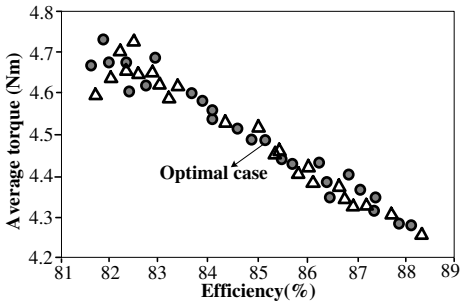

Fig. 26. Optimization results of last two generations.

B. Design optimization

Design optimization is performed to find optimal dimension parameters. An intelligent algorithm, namely genetic algorithm (GA) is adopted and then communicate with Maxwell to realize combined optimization [24-25]. GA has three operation factors, reproduction, crossover and mutation. Reproduction generates most adaptive individuals, when crossover and mutation mainly expand searching scope. The initialization of GA is performed as, a population of 25 elements, maximum generation number of 20, crossover factor of 0.8 and mutation factor of 0.2. Fig. 25 presents the optimization flowchart. The maximum torque and efficiency are two optimization objectives. Torque ripple ratio less than 10% is set as the optimization restriction.

During this optimization, the air gap length is fixed at 0.5mm and the current density is fixed at 7A/mm^2. The optimal ratio of i_0 is searched for all the elements in each generation. Further, optimization results of last two generations are given in Fig. 26. The optimal solution is defined as in which the product of toque and efficiency arrives the maximum value. The final parameters are listed in Table V. After optimization, about 4.5 Nm average torque and 84% efficiency is achieved under 16% i_0 injection.

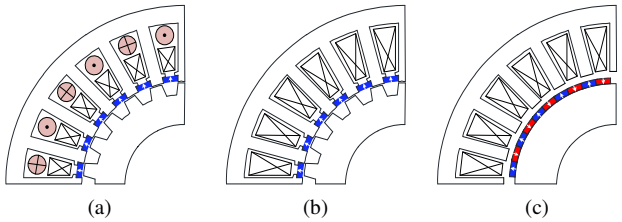

Fig. 27. (a) Existing VRM with separated AC and DC coils [22]. (b) Proposed VRM with integrated AC and DC coils. (c) Traditional SPM.

TABLE VI
Performance comparison for three machines

Parameters	Unit	Existing VRM	Proposed VRM	Traditional SPM
Outer diameter	mm	120	120	120
Stack length	mm	50	50	50
Air gap length	mm	0.5	0.5	0.5
Stator slot number	-	24	24	24
Rotor pole pairs	-	22	22	22
PM volume	mm^3	10500	10500	10500
AC copper loss	W	20	34	40
DC copper loss	W	20	6	-
Rated torque	Nm	3.4	4.6	5.1
Rated Efficiency	%	78	85	88
Flux weakening	-	Good	Good	Poor
PM demagnetization	-	No	No	Yes
Rotor robustness	-	Good	Good	Poor

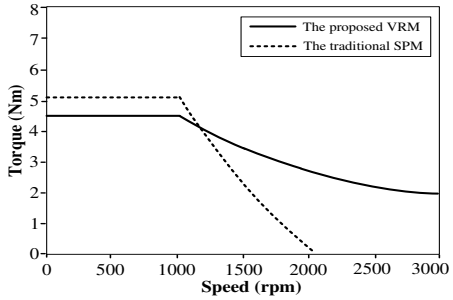

Fig. 28. Comparison of flux weakening performance.

C. Comparative study

A performance comparison is given between three different topologies as shown in Fig. 27. One is the existing VRM with separated AC and DC field windings. Another is the proposed VRM equipped with integrated AC and DC windings. The other is the traditional SPM excited by alternating rotor PMs. For a fair comparison, the machine dimensions, materials types, rotor pole pairs, PM volume and the whole copper loss are all kepted the same in three designs. Each design is individually optimized by GA and Maxwell combined method as discussed previously, to achieve optimal torque and efficiency performance.

The design parameters and calculated performance for three topologies are listed in Table VI. It is shown the proposed VRM with integrated AC and DC windings can achieve higher torque and efficiency compared to the existing topology with extra DC field winding. Compared to traditional SPMs, the torque and efficiency of the proposed design are slightly lower. However, its flux weakening ability is much better as denoted in Fig. 28. Moreover, in the proposed machine, PM demagnetization risk is avoided due to the unique PM arrangement in slots. Its rotor mechanical strength is also improved. It can be concluded that the proposed machine has a better robustness than traditional SPMs in both electromagnetic and mechanical aspects.

This article has been accepted for publication in a future issue of this journal, but has not been fully edited. Content may change prior to final publication. Citation information: DOI 10.1109/TIE.2019.2920600, IEEE Transactions on Industrial Electronics

(a) (b) (c)

Fig. 29. Protype details. (a) Stator lamination. (b) Stator assembly. (c) Rotor.

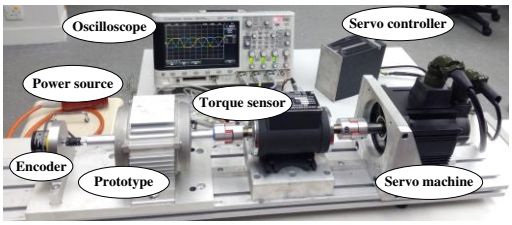

Fig. 30. Experimental platform based on the assembled prototype.

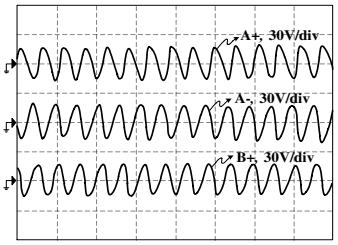

Fig. 31. No-load back emf at 1000 rpm

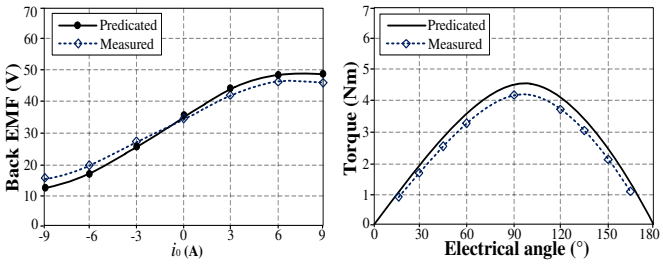

(a) (b)

Fig. 32. (a) Back emf curve against i_0 . (b) Static torque angle curve.

VI. Experimental Verification

To verify the feasibility of the proposed machine, a prototype is manufactured as shown in Fig. 29. The prototype parameters are in line with finite element modeling, as presented in Table II and Table V. Fig. 30 shows the experimental platform, which mainly consists of the prototype, a servo motor, torque sensor, DC power source, drive controller and oscilloscope.

The no-load back emf of sub-phases at speed 1000 rpm is plotted in Fig. 31. The back emf of two adjacent sub-phases has 180° electrical angle difference, and their distortion trends are opposite. Then, the back emf value against different i_0 is further collected as given in Fig. 32(a), which proves the bidirectional flux regulation ability of i_0. By injecting constant current into the armature winding and testing torque value at different rotor positions, torque angle curve is obtained as given in Fig. 32(b). The errors between tested results and finite element predication are acceptable considering manufacturing tolerance.

The on-load experiments are conducted with different current control strategies. When there is only i_q current injected into the armature winding, steady current and output torque are shown in Fig. 33(a). It can be found, fed by dual independent inverters, good current control effect can be achieved for each sub-phase, and steady torque can be generated. After that, combined i_q and

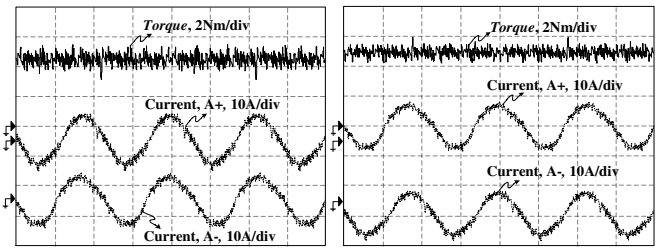

(a) (b)

Fig. 33. Steady current and torque. (a) Without i_0. (b) With 15% i_0.

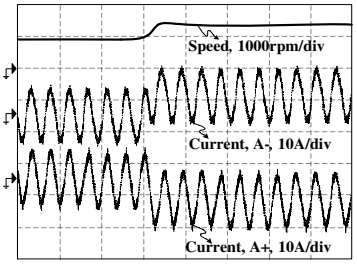

Fig. 34. Flux weakening operation by negative i_0 injection.

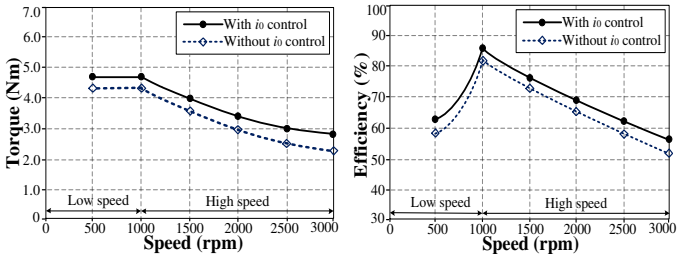

(a) (b)

Fig. 35. (a) Torque speed curves. (b) Efficiency speed curves.

i_0 are injected into the armature winding. The synthetic value of two current components keeps unchanged compared with that when only i_q is injected. The optimal ratio of i_0 is achieved by searching the point at which output torque arrives the maximum value. Fig. 33(b) shows steady current and torque waveforms with 15% injection ratio of i_0. The output torque is enhanced by about 10% compared to that with only i_q injection, thus proving the torque boost effect of i_0 and i_q combined control. Then, the flux weakening operation is performed at base speed 1000 rpm. As shown in Fig. 34, with negative i_0 injection, flux weakening effect and speed extension can be achieved as predicated.

Finally, the torque-speed curves are evaluated with different control strategies. The voltage restriction of DC supply is 160V. When the machine operates under the base speed, the constant torque control is applied with optimal i_0 injected. When it runs over the base speed. Flux weakening operation is applied for speed extension. Two flux weakening strategies are considered in this paper. One is by applying negative i_d for flux weakening, similar with that in conventional PM machine. The other is by applying both i_d and i_0 for combined flux weakening operation. The i_d directly control the PM magnetic field, while the i_0 gives parallel flux component. The tested torque and efficiency are plotted in Fig. 35. It can be found higher torque and efficiency can be achieved in the whole speed region with extra i_0 control. The efficiency improvement is due to torque boost effect as well as loss mitigation with extra i_0 control. In general, the proposed machine achieves improved performance with i_0 control in both low-speed and high-speed regions, which proves it a potential candidate for electric vehicle propulsion.

This article has been accepted for publication in a future issue of this journal, but has not been fully edited. Content may change prior to final publication. Citation information: DOI 10.1109/TIE.2019.2920600, IEEE Transactions on Industrial Electronics

VII. CONCLUSION

With the increasing concern of high-performance propulsion machines for the modern electric vehicles, this paper proposes a new Vernier reluctance machine with AC and DC integrated winding, which owns the advantages of a robust rotor structure, good torque density and flexible flux control capacity. This new machine employs slot PMs as the dominating source for torque generation based on the flux modulation mechanism. Further, zero-sequence current excitation is injected to boost its torque density and mitigate torque ripple. Meanwhile, zero-sequence current excitation can serve as an additional control variable for flux weakening and speed extension. In this paper, the machine structure, operation principle and its integrated drive method are introduced in detail. The feasibility of the proposed machine is verified by both finite element analysis and prototype testing. Leading design parameters are analyzed and optimized to give a design guideline for this new machine. This paper reveals that, with 10% to 20% injection ratio of zero-sequence current, the proposed machine can achieve about 10% torque density boost and 30% torque ripple reduction. Meanwhile, core loss and PM eddy current loss can be distinctly mitigated with zero-sequence current injection, thus leading to efficiency increase. However, with the use of a dual-inverter system, the increased complexity of drive circuit and control strategy are disadvantageous for this new machine. Future works, for instance, developing potential fault-tolerant capacity under this drive structure, could help to balance the system cost and machine performance.

REFERENCE

[1] S. U. Chung, S. H. Moon, D. J. Kim and J. M. Kim, "Development of a 20-Pole-24-Slot SPMSM with consequent pole rotor for in-wheel direct drive," *IEEE Trans. Ind. Electron.*, vol. 63, no. 1, pp. 302-309, Jan. 2016.

[2] J. Nerg, M. Rilla, V. Ruuskanen, J. Pyrhönen, and S. Ruotsalainen, "Direct-driven interior magnet permanent-magnet synchronous motors for a full electric sports car," *IEEE Trans. Ind. Electron.*, vol. 61, no. 8, pp. 4286–4294, Aug. 2014.

[3] P. B. Reddy, A. M. El-Refaie, K. K. Huh, J. K. Tangudu and T. M. Jahns, "Comparison of interior and surface PM machines equipped with fractional-Slot concentrated windings for hybrid traction applications," *IEEE Trans. Energy Convers,* vol. 27, no. 3, pp. 593-602, Sept. 2012.

[4] K. Yamazaki and M. Kumagai, "Torque analysis of interior permanent magnet synchronous motors by considering cross-magnetization: Variation in torque components with permanent-magnet configurations," *IEEE Trans. Ind. Electron.*, vol. 61, no. 7, pp. 3192–3201, Jul. 2014.

[5] D. K. Hong, W. Hwang, J. Y. Lee and B. C. Woo, "Design, analysis, and experimental validation of a permanent magnet synchronous motor for articulated robot applications," *IEEE Trans on Magn.*, vol. 54, no. 3, pp. 1-4, March 2018.

[6] M. M. Swamy, T. Kume, A. Maemura, S. Morimoto, "Extented high-speed operation via electronoic winding-change." *IEEE Trans. Ind. Appl.*, vol. 42, no. 3, pp. 742-752. 2006.

[7] A. M. El-Refaie, T. M. Jahns, P. J. McCleer and J. W. McKeever, "Experimental verification of optimal flux weakening in surface PM Machines using concentrated windings," *IEEE Trans. Ind. Appl.*, vol. 42, no. 2, pp. 443-453, 2006.

[8] S. U. Chung, J. W. Kim, Y. D. Chun, B. C. Woo, and D. K. Hong, "Fractional slot concentrated winding PMSM with consequent pole rotor for a low-speed direct drive: Reduction of rare earth permanent magnet" *IEEE Trans. Energy Convers.*, vol. 30, no. 1, pp. 103–109, Mar. 2015.

[9] J. Li, K. Wang and F. Li, "Analytical prediction of optimal split ratio of consequent-pole permanent magnet machines," *IET Electric Power Appl*, vol. 12, no. 3, pp. 365-372, 3 2018.

[10] S. U. Chung, J. W. Kim, and D. H. Koo, "A novel design of modular three-phase permanent magnet Vernier machine with consequent pole rotor," *IEEE Trans. Magn*., vol. 47, no. 10, pp. 4215-4218, 2011.

[11] D. Li, R. Qu, J. Li, L. Xiao, L. Wu, and W. Xu "Analysis of torque capability and quality in Vernier permanent magnet machines," IEEE Trans. Ind. Appl., vol. 52, no. 1, pp.125-135, 2016.

[12] K. T. Chau, C. C. Chan and C. Liu, "Overview of permanent-magnet brushless drives for electric and hybrid electric vehicles," *IEEE Trans. Ind. Electron.*, vol. 55, no. 6, pp. 2246-2257, 2008.

[13] M. Cheng, W. Hua, J. Zhang and W. Zhao, "Overview of stator-permanent magnet brushless machines," *IEEE Trans. Ind. Electron.*, vol. 58, no. 11, pp. 5087-5101, Nov. 2011.

[14] A. Fasolo, L. Alberti and N. Bianchi, "Performance comparison between switching-flux and IPM machines with rare-earth and ferrite PMs," *IEEE Trans. Ind. Appl*, vol. 50, no. 6, pp. 3708-3716, Nov.-Dec. 2014.

[15] Z. Z. Wu, Z. Q. Zhu, "Analysis of air-gap field modulation and magnetic gearing effects in switched flux permanent magnet machines", *IEEE Trans. Magn.*, vol. 51, no. 5, May 2015.

[16] Y. Chen, W.N. Fu, and X. Weng: 'A concept of general flux-modulated electric machines based on a unified theory and its application to developing a novel doubly-fed dual-stator motor', *IEEE Trans. Ind. Electron.*, vol. 64, no. 12, pp. 9914-9923, 2017.

[17] X. Zhao and S. Niu, "Design and optimization of a new magnetic-geared pole-changing hybrid excitation machine," *IEEE Trans. Ind. Electron.,* vol. 64, no. 12, pp. 9943-9952, Dec. 2017.

[18] D. S. More and B. G. Fernandes, "Analysis of flux-reversal machine based on fictitious electrical gear," *IEEE Trans. Energy Convers.*, vol. 25, no. 4, pp. 940-947, Dec. 2010.

[19] Z. Z. Wu and Z.Q. Zhu, "Analysis of magnetic gearing effect in partitioned stator switched flux PM machines," *IEEE Trans. Energy Convers.*, vol.31, no.4, pp.1239-1249, 2016.

[20] Y. Gao, R. Qu, D. Li, J. Li and G. Zhou, "Consequent-pole flux-reversal permanent-magnet machine for electric vehicle propulsion," *IEEE Trans. Appl. Supercond*, vol. 26, no. 4, pp. 1-5, 2016.

[21] L. Shao, W. Hua, Z. Q. Zhu, X. Zhu, M. Cheng and Z. Wu, "A novel flux-switching permanent magnet machine with overlapping windings," *IEEE Trans on Energy Convers*, vol. 32, no. 1, pp. 172-183, 2017.

[22] X. Zhao and S. Niu, "Design of a novel parallel-hybrid-excited Vernier reluctance machine with improved utilization of redundant winding harmonics," *IEEE Trans. Ind. Electron,* vol. 65, no. 11, pp. 9056-9067, Nov. 2018.

[23] Z. Q. Zhu and B. Lee, "Integrated field and armature current control for dual three-phase variable flux reluctance machine drives," *IEEE Trans on Energy Convers.,* vol. 32, no. 2, pp. 447-457, June 2017.

[24] X. Zhao and S. Niu "Design and optimization of a novel slot-PM-assisted variable flux reluctance generator for hybrid electric vehicles," *IEEE Trans on Energy Convers*, vol, no. 99, pp. 1-1,2018.

[25] K. J. Han, D. H. Cho, and H. K. Jung, "Optimal core shape design for cogging torque reduction of BLDC motor using genetic algorithm," *Proc. Compumag.*, Sapporo, Japan, 1999, pp. 332–333.

Xing Zhao received the B.Sc. degree from the Department of Automation at Nanjing University of Aeronautics and Astronautics, China, in 2014, and currently he is pursuing Ph.D. degree in the department of Electrical Engineering at the Hong Kong Polytechnic University, Hong Kong. His research fields include design and control of novel electric machines for EV/HEVs and renewable energy systems.

Shuangxia Niu received the B.Sc. and M.Sc. degrees from Tianjin University, China, in 2002 and 2005, respectively, and the Ph.D. degree from the University of Hong Kong, Hong Kong, in 2009, all in electrical engineering. Currently she is an Associate Professor in the Department of Electrical Engineering with the Hong Kong Polytechnic University. She has authored over 90 published journal papers and is the holder of 6 patents. Her research includes machine design and renewable energy conversion.